Research Square

Preprints are preliminary reports that have not undergone peer review.
They should not be considered conclusive, used to inform clinical practice,
or referenced by the media as validated information.

Preparation of Sn/Na-Co3O4 Nanospheres for Improved Triethylamine Sensing Performance Research

Yuhong Zhang
Jilin jianzhu university
Junnan Liu
Jilin jianzhu university
Haoran Niu
Jilin jianzhu university
Juncheng Li
Jilin jianzhu university
Mingzhe Cui
Jilin jianzhu university
Hang Liu
liuhang76@163.com
Jilin jianzhu university

Research Article

Keywords: Co3O4, Nanospheres, gas response, triethylamine

Posted Date: November 20th, 2026

DOI: https://doi.org/10.21203/rs.3.rs-11629369/v1

License: This work is licensed under a Creative Commons Attribution 4.0 International License.
Read Full License

Additional Declarations: No competing interests reported.

Preparation of Sn/Na-Co_3O_4 Nanospheres for Improved Triethylamine Sensing Performance Research

Yuhong Zhang[a], Junnan Liu[a], Haoran Niu[a], Juncheng Li[a], Mingzhe Cui[a], Hang Liu[a,b]*
a.School of electrical and computer engineering, Jilin jianzhu university, Changchun
b.Jilin Provincial Key Laboratory of Fire Risk Prevention and Emergency Rescue for Building, Changchun,130000, China
*Corresponding author: liuhang76@163.com

Abstract

Here, a series of Sn/Na co-doped Co_3O_4 nanospheres are synthesized by a one-step solvothermal method. The gas sensing performance of Co_3O_4-based nanospheres toward triethylamine is investigated in detail. The optimal operating temperature of 1%Sn5%Na-Co_3O_4 nanospheres to 100 ppm triethylamine is lower 20 ℃ than that of pure Co_3O_4. Compared with pure Co_3O_4, the response of 1%Sn5%Na-Co_3O_4 nanospheres is increased by approximately 7.2 times. Furthermore, the 1%Sn5%Na-Co_3O_4 sensor exhibits better anti-humidity and lower detection limit. At last, the possible gas mechanism is discussed according to the modulation of the Co_3O_4 microstructure and surface chemistry by co-doping Sn/Na. Therefore, the Sn/Na-Co_3O_4 nanospheres offer new insights for the design of triethylamine sensors and provide potential application in food safety monitoring and the early detection of fish spoilage.

Keywords: Co_3O_4, Nanospheres, gas response, triethylamine

1. Introduction

Fish and other aquatic products, rich in high-quality protein, unsaturated fatty acids, and various micronutrients, have gradually become an indispensable source of nutrition in people's daily diets[1]. As a major component of seafood, fish is highly susceptible to spoilage and deterioration due to microbial activity and endogenous enzymatic degradation during harvesting, transportation, storage, and sale[2]. Following fish death, endogenous enzymatic activity and microbial growth gradually accelerate the degradation of proteins, amino acids, and other nitrogen-containing compounds, leading to the formation and release of various volatile nitrogen-containing compounds during spoilage[3]. As spoilage progresses, volatile amines such as triethylamine (TEA) are continuously released, and their concentrations generally increase with prolonged storage time[4]. Owing to its high volatility and pungent odor, TEA is considered an important volatile marker for evaluating fish freshness. According to the report, when the fish is stored at 25 ℃ condition, the 1.0974 ppm TEA are released from the fish after two days. Especially, the TEA concentration will increase progressively to 2.8498, 5.4731, 6.9352, 9.2574, 12.316 and 15.3263 ppm after four, six, eight, ten, twelve and fourteen days, respectively. The storage time of fish is over four days, the fish presents severe spoilage[5]. Therefore, the detection of TEA concentration attribute to realize the fish freshness[6]. Generally, the main methods for detecting TEA gas include gas chromatography (GC) and gas chromatography-mass spectrometry (GC-MS)[7]. Although the methods can offer high accuracy and reliability, but they typically

require complex instrumentation, specialized operators and relatively cumbersome sample pretreatment procedures. These methods are not suitable for developing rapid and portable equipment. Therefore, the development of a compact, low-cost and high response gas sensor is a significance issue for the early identification of fish spoilage.

At present, the metal oxide semiconductor (MOS) gas sensors have attracted considerable attention for gas detection because of their high sensitivity, low cost and compatibility with miniaturized sensing devices[8]. A series of metal oxides, such as SnO_2, ZnO, In_2O_3, WO_3 and CuO, have been investigated as sensing materials for TEA detection. In 2023, Liu et al. reported that Pt_1/ZnO nanorods could serve as an effective sensing material for TEA detection. The sensor exhibited a remarkable response of 4170 to 100 ppm TEA at 200 ℃, which was approximately 92 times higher than that of pure ZnO[9]. Gui et al. demonstrated that flower-like WO_3 materials shown a response of 180.7 to 100 ppm TEA[10]. In addition, Liu et al. reported that porous CuO with abundant surface oxygen vacancies showed a high response of 140.0 to 50 ppm TEA and good selectivity toward TEA even at room temperature[11]. These results have further highlighted the potential application of MOS sensor for TEA detection.

Co_3O_4 is a typical p-type MOS with a spinel crystal structure, containing both Co^{2+} and Co^{3+} ions in its lattice[12]. In 2022, Kong et al. reported that the lower-coordination Co_3O_4 mesoporous hierarchical microspheres exhibited a response of 34.1 to 100 ppm TEA at 150 ℃ and a detection limit as low as 0.5 ppm[13]. In 2024, Ding et al. reported that the coral flower-like Fe-doped Co_3O_4 materials exhibited a response 21.2 toward 100 ppm TEA at 199 ℃, approximately five times higher than that of pristine Co_3O_4[14]. These studies demonstrate that the Co_3O_4 material can be used to detect TEA.

In practical gas-sensing applications, pure Co_3O_4 still suffers from issues such as limited response values, high operating temperature and insufficient surface active sites[15]. Generally, the elemental doping or the formation of hetero junctions are among the effective methods for improving the gas-sensing performance of MOS materials[16]. Therefore, the dopant of element is an effective modification strategy for improving the gas-sensing performance of Co_3O_4. Zhang et al. reported that mesoporous Sn-doped Co_3O_4 whiskers exhibited enhanced sensing performance toward toluene at 240 ℃, with a response approximately 7.6 times higher than that of pristine Co_3O_4[17]. In 2024, Saad et al. reported Li/Na co-doped Co_3O_4 thin films, which exhibited enhanced sensing performance toward CO_2 at room temperature, with a response of 345.01% to 9990 ppm CO_2 at 30 ℃, approximately 6.9 times higher than that of 3%Li-Co_3O_4[18]. Compared to single doping, co-doping sample is expected to further optimize the surface defect structure, active oxygen content and charge carrier transport properties of Co_3O_4 host, thereby enhancing its gas-sensing response. To our knowledge, the Na/Sn-doped Co_3O_4 materials are not reported.

Here, the Sn/Na co-doped Co_3O_4 nanospheres are prepared by a one-step solvothermal method. The crystal structure, specific surface area, elemental composition and surface chemical state of the material were systematically analyzed to investigate the effects of Sn and Na doping Co_3O_4. The gas-sensing properties of the Sn/Na-Co_3O_4 materials toward TEA were systematically investigated. In addition, the gas-sensing mechanism was analyzed based on the structural characteristics and surface chemical state of the material. The research provides an effective approach for developing Co_3O_4-based TEA sensor with high response, low detection limit and good stability. It also offers potential applications for the early detection of fish spoilage and rapid monitoring of food safety.

2. Experimental

2.1. Chemical material

The raw materials include cobalt nitrate hexahydrate ($Co(NO_3)_2 \cdot 6H_2O$, 99 %, Aladdin), tin chloride pentahydrate ($SnCl_4 \cdot 5H_2O$, 99 %, Aladdin), sodium nitrate solution ($NaNO_3$, 99 %), isopropanol (C_3H_8O, 99.9 %, Aladdin) and glycerol ($C_3H_8O_3$, 99.5 %, Aladdin).

2.2. Preparation of Co3O4, Sn-Co3O4, Na-Co3O4 and Sn/Na-Co3O4

All composite materials are synthesized through one-step solvothermal method. The detail process is illustrated in Fig. 1. First, 0.291 g $Co(NO_3)_2 \cdot 6H_2O$ is dissolved in 30 mL C_3H_8O and stirred for 30 minutes to obtain solution 1. Next, 8 mL $C_3H_8O_3$ is added to solution 1, then stirring for 2 h. The solution 1 is transferred to a 50 mL Teflon-lined stainless steel high-pressure vessel, sealed and reacted at 180 ℃ for 6 h. The obtained product is washed alternately with deionized (DI) water and ethanol, then centrifuged and dried at 80 ℃ for 8 h. The dried precursor is ground, then calcined at 500 ℃ with a heating rate of 5 ℃/min for 2 h to obtain Co_3O_4 powder. The preparation methods for Sn-Co_3O_4, Na-Co_3O_4 and Sn/Na-Co_3O_4 are similar to those for pure Co_3O_4. x g of $SnCl_4 \cdot 5H_2O$ (x = 0.0018, 0.0026, 0.0035, 0.0044) is added to 1 mL DI water and ultrasonated at room temperature until completely dissolved to obtain the solution 2. Then the solution 2 is added to solution 1; the remaining steps are identical to those for synthesizing pure Co_3O_4. At last the x%Sn-Co_3O_4 (x = 0.5, 0.75, 1, 1.25) composites are obtained. Next, y mol% $NaNO_3$ (y = 4, 5, 6, 7) is dissolved in 1 mL DI water to obtain solution 3. The solution 3 is mixed into solution 1, and the remaining steps are identical to the synthesis method for pure Co_3O_4. The y%Na-Co_3O_4(y = 4, 5, 6, 7) materials are obtained, respectively. The synthesis of Sn/Na-Co_3O_4 follows the same method as described above.

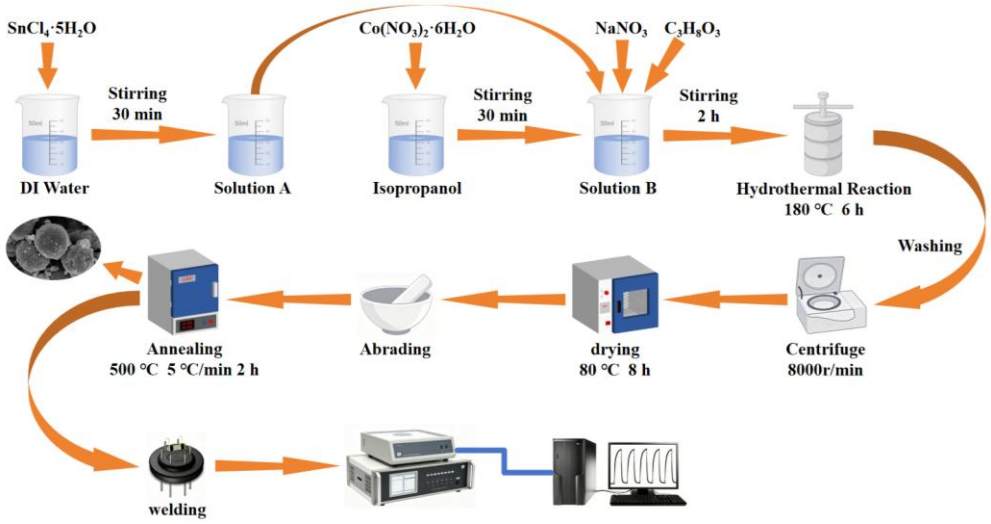


Fig. 1. Synthesis procedure of Sn/Na-Co_3O_4 nanomaterials.

2.3. Preparation and gas-sensing testing of sensors

The calcined powders are mixed with ethanol and DI water, ground into a homogeneous paste. Then the powders are uniformly coated onto an alumina ceramic tube. The coated ceramic tube is calcined at 500 ℃ for 2 h. The ceramic tube is soldered with a base and a pair heating wire. The sensor is obtained. And the sensor is aged at 180 ℃ for 48 h. Finally, the sensor is tested for the target gas. The sensitivity response (S) of the prepared gas-sensitive element is defined as $S = R_g/R_a$, where R_a is the resistance of the sensor in air and R_g is the resistance of the sensor in the target gas.

2.4. Characterization

The phase composition of the samples was analyzed by an X-ray diffractometer (XRD, Rigaku Ultima IV) in the 2θ range of 20-70°, with a step size of 0.02°. The morphological characteristics of all samples were observed using a scanning electron microscope (SEM, Zeiss Sigma 360) at 5.0 kV. The morphology and lattice fringes of 1%Sn5%Na-Co_3O_4 were observed by high-resolution transmission electron microscopy (HRTEM, JEOL F200). X-ray photoelectron spectroscopy (XPS, Zeiss Sigam 360) was used to determine the elemental composition and chemical state. The specific surface area and nitrogen adsorption-desorption curves of the samples were measured using a fully automated specific surface area analyzer (BET, Kanta Autosorb IQ). The gas sensitivity of all samples was tested using a CGS-8 intelligent gas sensitivity analyzer.

3. Results and discussion

3.1. Structure characterization

The XRD patterns of pure Co_3O_4, 1%Sn-Co_3O_4, 5%Na-Co_3O_4 and 1%Sn5%Na-Co_3O_4 are shown in Fig. 2. The five obvious diffraction peaks are obtained at 31.27°, 36.84°, 44.80°, 59.35° and 65.23°, corresponding to the (220), (311), (400), (511) and (440) crystal planes, respectively. The positions of the diffraction peaks for each sample are essentially consistent with the standard diffraction peaks of spinel-type Co_3O_4, indicating that the samples all retain the main crystal structure of Co_3O_4[19]. At the same time, no obvious diffraction peaks corresponding to SnO_2, Na_2O, Na_2CO_3 and other crystalline impurity phases are obtained. The results indicate that the Sn and Na are well dispersed within the samples. The XRD patterns of other Sn-Co_3O_4, Na-Co_3O_4 and Sn/Na-Co_3O_4 with different doping concentrations are shown in Figure S1. The diffraction peaks of all samples also are basically consistent with the standard diffraction peaks of Co_3O_4.

In Fig. 3(a-d), the XRD results of pure Co_3O_4, 1%Sn-Co_3O_4, 5%Na-Co_3O_4 and 1%Sn5%Na-Co_3O_4 are refined by GSAS-II. The corresponding refinement results are summarized in Table 1. The R_{wp} values range from 2.316 % to 2.703 %, while the GOF and χ^2 values range from 1.27 to 1.32 and from 1.62 to 1.72, respectively. For all samples, the refined lattice parameters show $a = b = c$ with $\alpha = \beta = \gamma = 90°$, which confirm that the cubic spinel structure of Co_3O_4 is retained with doping Sn, Na and Sn/Na. The refined lattice constants and unit-cell volumes of the doped samples are slightly larger than those of pure Co_3O_4. This slight variation indicates that the incorporation of Sn and Na produces lattice expansion without altering the cubic symmetry of the Co_3O_4 structure.

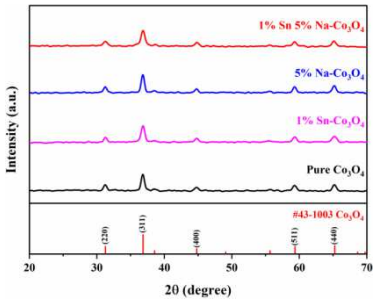


Fig. 2. XRD patterns of the four samples.

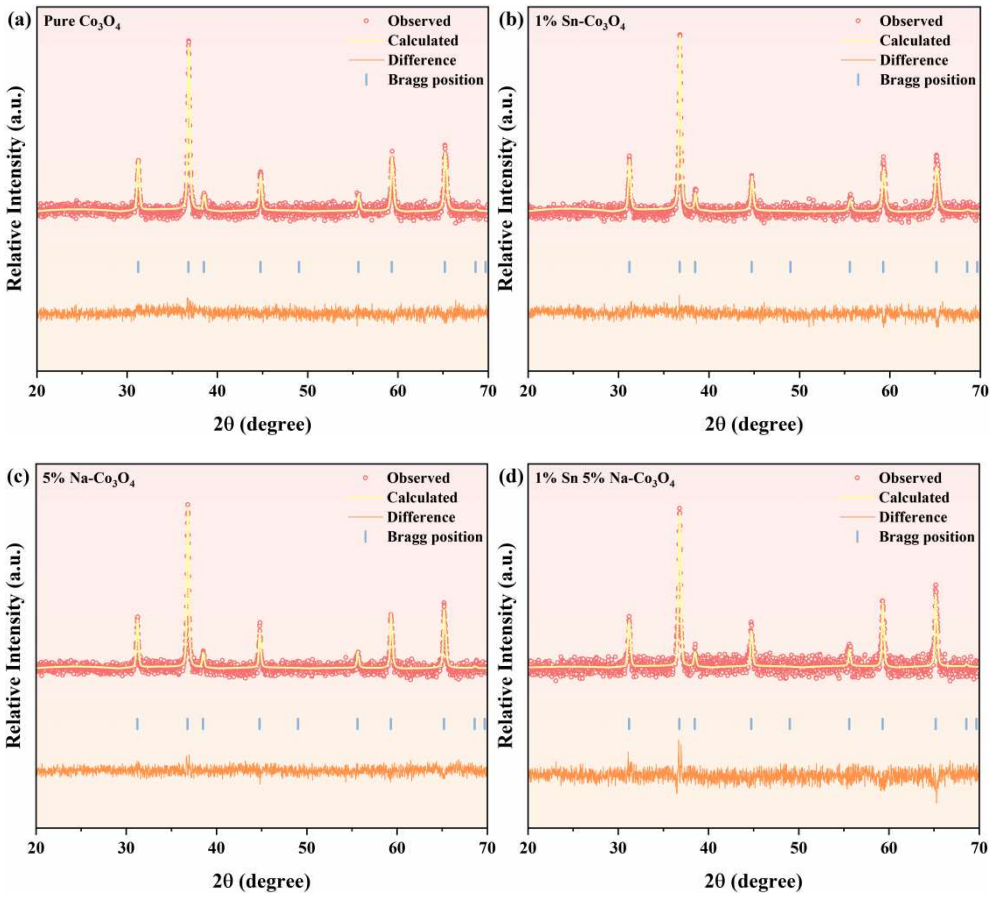


Fig. 3. (a-d) Rietveld refinement results of pure Co_3O_4, 1%Sn-Co_3O_4, 5%Na-Co_3O_4 and 1%Sn5%Na-Co_3O_4, respectively.

Table.1 Refined structural data for all samples.

Sample	Pure Co_3O_4	1%Sn-Co_3O_4	5%Na-Co_3O_4	1%Sn5%Na-Co_3O_4
a = b = c (Å)	8.07859	8.08370	8.07931	8.08054
Volume (Å^3)	527.238	528.239	527.380	527.620
α = β = γ (°)	90	90	90	90
χ^2	1.62	1.72	1.70	1.62
GOF	1.27	1.32	1.30	1.27
R_{wp} (%)	2.316	2.413	2.511	2.703

The SEM images of pure Co_3O_4, 1%Sn-Co_3O_4, 5%Na-Co_3O_4 and 1%Sn5%Na-Co_3O_4 nanomaterials are shown with a scale bar of 1 μm in Fig. 4(a-d). The pure Co_3O_4 sample exhibits a spherical morphology with a certain degree of particle agglomeration and relatively rough surfaces. In contrast, the 1%Sn5%Na-Co_3O_4 sample exhibits a more uniform spherical morphology with smoother surfaces and clearer particle contours than pure Co_3O_4. Furthermore, the average particle size of all samples is estimated by Nano Measurer software. The average particle sizes of pure Co_3O_4, 1%Sn-Co_3O_4, 5%Na-Co_3O_4 and 1%Sn5%Na-Co_3O_4 are approximately 731, 686, 729 and 669 nm, respectively. So the particle sizes of all doping samples are smaller than that of pure Co_3O_4.

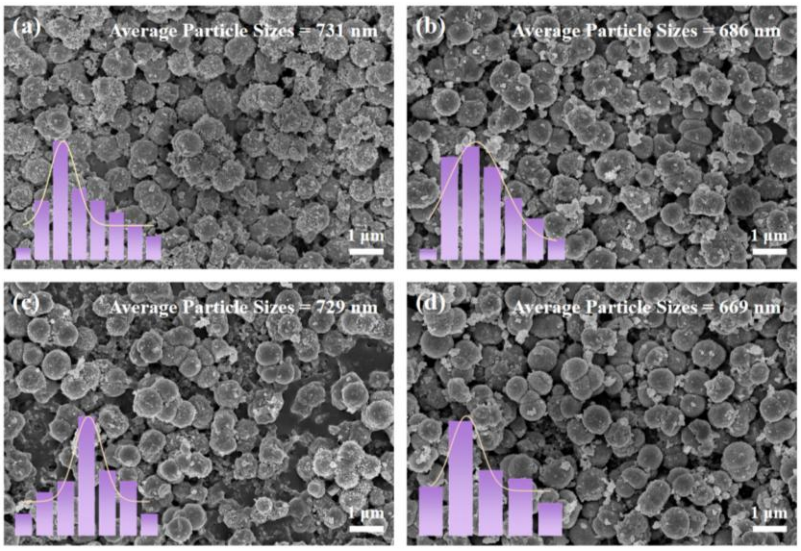


Fig. 4. SEM images of different samples: (a) Pure Co_3O_4; (b) 1%Sn-Co_3O_4; (c) 5%Na-Co_3O_4; (d) 1%Sn5%Na-Co_3O_4.

The microstructure and elemental distribution of the 1%Sn5%Na-Co_3O_4 nanospheres are characterized through TEM, HRTEM and EDS mapping. As shown in Fig. 5(a-b), the TEM images of the 1%Sn5%Na-Co_3O_4 nanospheres are obtained at different magnifications. The sample exhibits a distinct spherical morphology with well-defined particle contours, and the nanospheres have a diameter of approximately 670 nm. Fig. 5(c) shows the HRTEM image, in which clear lattice fringes are observed. The measured interplanar spacing is 0.286 nm, which corresponds to the (220) plane of the cubic spinel Co_3O_4. It indicates that the 1%Sn5%Na-Co_3O_4 sample retains the crystal structure characteristics of Co_3O_4, consistent with the analysis of the Co_3O_4 primary phase in the XRD results. The elemental distribution of 1%Sn5%Na-Co_3O_4 is further analyzed via EDS mapping. As shown in Fig. 5(d-h), the distribution regions of Co, O, Sn, and Na are all circular and generally coincide with the spherical particle contours observed in the TEM images. Among these, Co and O belong to the main constituent elements of Co_3O_4, which are distributed throughout the entire spherical particle region. The Sn and Na are also distributed within this spherical region, indicating a good spatial correspondence between Sn and Na and the Co_3O_4 matrix.

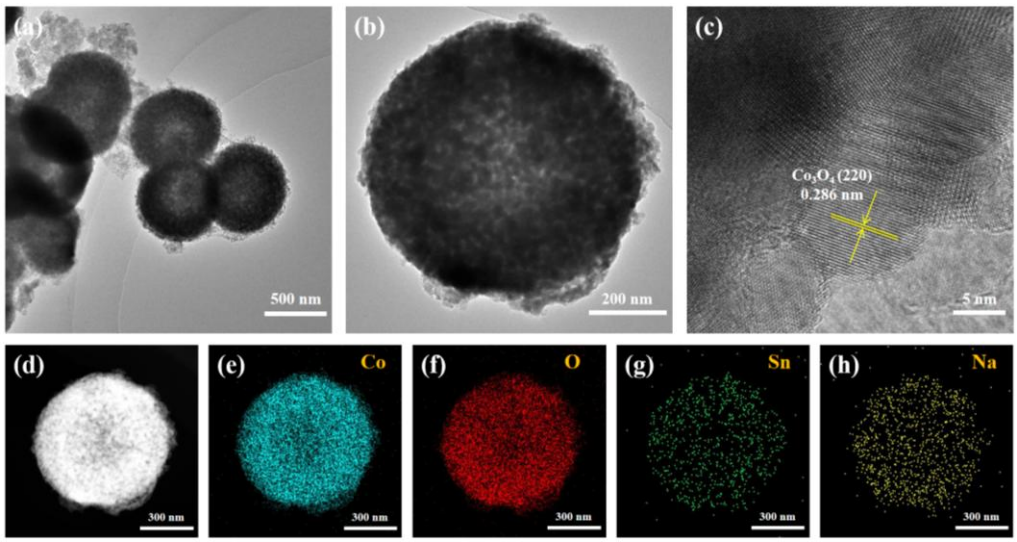


Fig. 5. (a-b) TEM images of 1%Sn5%Na-Co_3O_4 at different magnifications; (c) HRTEM image of 1%Sn5%Na-Co_3O_4; (d-h) EDS elemental mapping images of 1%Sn5%Na-Co_3O_4.

The elemental composition and surface chemical states of pure Co_3O_4 and 1%Sn5%Na-Co_3O_4 samples are analyzed by XPS. The XPS survey spectra of two samples are shown in Fig. 6(a), the main signals include Co, O, and C for pure Co_3O_4; the C 1s peak typically originates from the adsorption of hydrocarbons from air onto the sample surface during the testing process. In contrast, the 1%Sn5%Na-Co_3O_4 sample exhibits not only the characteristic peaks of Co, O and C, but also signals associated with Sn and Na, indicating that Sn and Na are successfully introduced into the Co_3O_4 sample.

The high-resolution Co 2p spectra of two samples are shown in Fig. 6(b). Two samples also exhibit two main characteristic peaks, Co $2p_{1/2}$ and Co $2p_{3/2}$, accompanied by corresponding satellite peaks. Based on the results of fitting shape, the Co 2p spectrum can be further decomposed into two valence state components: Co^{2+} and Co^{3+}[20]. It indicates the simultaneous presence of tetrahedral Co^{2+} and octahedral Co^{3+} in the two samples, consistent with the typical chemical characteristics of spinel Co_3O_4. In pure Co_3O_4, the Co $2p_{1/2}$ and Co $2p_{3/2}$ peaks are located at 794.7 and 779.7 eV, respectively. The spin-orbit splitting energy difference is approximately 15.0 eV. In 1%Sn5%Na-Co_3O_4, the Co $2p_{1/2}$ and Co $2p_{3/2}$ peaks are located at 794.8 and 779.8 eV, respectively. Compared with pure Co_3O_4, the Co 2p peak positions of 1%Sn5%Na-Co_3O_4 show only a slight shift of 0.1 eV, which indicates the doping Sn/Na does not significantly alter the main valence structure of Co_3O_4. The high-resolution Sn 3d and Na 1s spectra of 1%Sn5%Na-Co_3O_4 are shown in Fig. 6(c-d). The Sn $3d_{5/2}$ and Sn $3d_{3/2}$ peaks located at approximately 486.8 and 495.2 eV, respectively, are characteristic of Sn^{4+}, indicating that Sn mainly exists in the Sn^{4+} state in the sample[21]. In the Na 1s spectrum, a characteristic peak is observed at approximately 1071.4 eV, corresponding to Na^+, indicating the successful introduction of Na into the sample[22]. The high-resolution O 1s spectra are further used to analyze the composition of oxygen species on the sample surface. As shown in Fig. 6(e-f), the O 1s spectrum is fitted to three components: lattice oxygen (O_L), oxygen vacancies (O_V) and chemically adsorbed oxygen (O_C)[23]. In the O 1s spectrum of pure Co_3O_4, the peak area ratios of O_L, O_V and O_C are 61.74%, 22.20% and 16.06%, respectively. In the that of 1%Sn5%Na-Co_3O_4, the peak area ratios of O_L, O_V and O_C are 53.17%, 25.68% and 21.15%, respectively. The 1%Sn5%Na-Co_3O_4 sample

shows a decreased proportion of O_L on the sample surface, while the contents of O_V and O_C increase. For MOS gas-sensing materials, the increase of O_V content enhances the adsorption of oxygen molecules on the sample surface, while the increased content of chemisorbed oxygen provides more active sites for the reaction between target gas molecules and surface oxygen species[24,25].

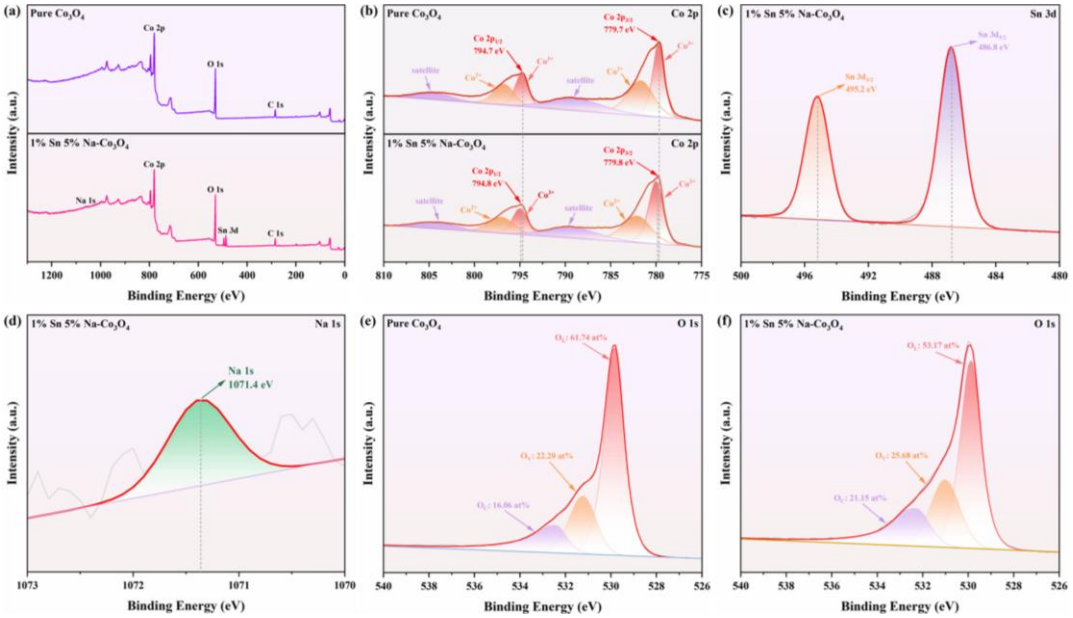


Fig. 6. (a) XPS survey spectra of pure Co_3O_4 and 1%Sn5%Na-Co_3O_4; (b) Co 2p spectra of two samples; (c) Sn 3d spectrum of 1%Sn5%Na-Co_3O_4; (d) Na 1s spectrum of 1%Sn5%Na-Co_3O_4; (e-f) O 1s spectra of two samples.

To investigate the effect of porous structure on the gas-sensing performance of the materials, N_2 adsorption-desorption tests are conducted on pure Co_3O_4 and 1%Sn5%Na-Co_3O_4 samples. As shown in Fig. 7(a-b). The results indicate that both samples exhibit typical Type IV adsorption-desorption isotherms, suggesting that the materials possess a mesoporous structure. The BET test results show that the specific surface area of pure Co_3O_4 is 23.242 m^2/g, while that of 1%Sn5%Na-Co_3O_4 increases to 31.675 m^2/g, indicating that doping effectively improves the porous structure and exposes more active surface sites. A larger specific surface area facilitates the adsorption and activation of oxygen molecules, while also providing more pathways for the diffusion and transport of gas molecules, thereby promoting reactions between gas molecules and surface-adsorbed oxygen[23].

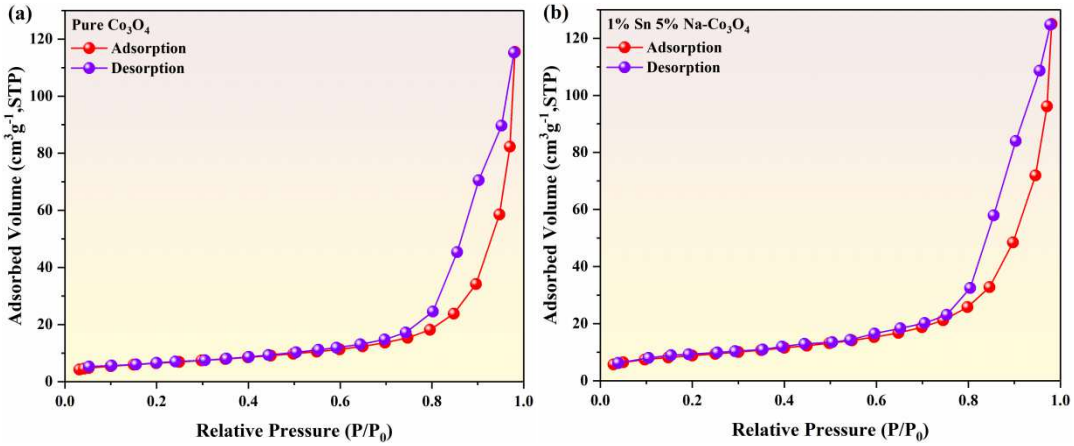


Fig. 7. (a-b) N_2 adsorption-desorption isotherms of pure Co_3O_4 and 1%Sn5%Na-Co_3O_4.

3.2 Gas sensing properties

To investigate the effect of doping on the gas-sensing performance of Co_3O_4-based materials, the response characteristics of pure Co_3O_4, Sn-Co_3O_4, Na-Co_3O_4 and Sn/Na-Co_3O_4 sensors toward 100 ppm TEA were evaluated at different operating temperatures. As shown in Fig. 8(a), the pure Co_3O_4 sensor reaches its maximum response 10.058 at 190 ℃. Compared with the pure Co_3O_4 sensor, the 1%Sn-Co_3O_4 sensor shows significantly improved gas-sensing performance, achieving a response value of approximately 61.981 at the optimal operating temperature of 190 ℃, which is about 6.1 times that of the pure Co_3O_4 sensor. The enhanced response of the Sn-Co_3O_4 sensor after Sn doping can be attributed to the reduced crystallite size and increased specific surface area caused by the incorporation of Sn^{4+} into the Co_3O_4 lattice, thereby exposing more sites for the adsorption of oxygen and TEA molecules[27]. Meanwhile, the doping Sn can regulate the hole concentration of p-type Co_3O_4 and increase the amount of surface-adsorbed oxygen species[28]. Consequently, more oxygen species participate in the reaction with TEA, inducing a larger resistance change and thus improving the gas-sensing response. As shown in Fig. 8(b), all Na-Co_3O_4 sensors reach their maximum responses at 170 ℃, which is 20 ℃ lower than the optimal operating temperature of pure Co_3O_4, while the 5%Na-Co_3O_4 sensor exhibits the highest response among the Na-doped samples. As shown in Fig. 8(c), the Sn/Na-Co_3O_4 sensors with different doping concentrations also reached their optimal operating temperature at 170 ℃. At this temperature, the 1%Sn5%Na-Co_3O_4 sensor achieved the highest response among all samples, with a response value of approximately 72.722, which was about 7.2 times that of the pure Co_3O_4 sensor. This indicates that the co-doping of Sn and Na has a significant synergistic enhancing effect on the gas-sensing performance of Co_3O_4. The temperature-dependent responses of four representative sensors are compared in Fig. 8(d). The results demonstrate that Sn/Na co-doping not only markedly enhances the TEA-sensing response but also shifts the optimal operating temperature toward a lower value, confirming the superior overall sensing performance of the co-doped sensor. The resistances of all samples are measured at different operating temperatures in Fig. 9(a-c). The resistance of all samples decreases with temperature increasing.

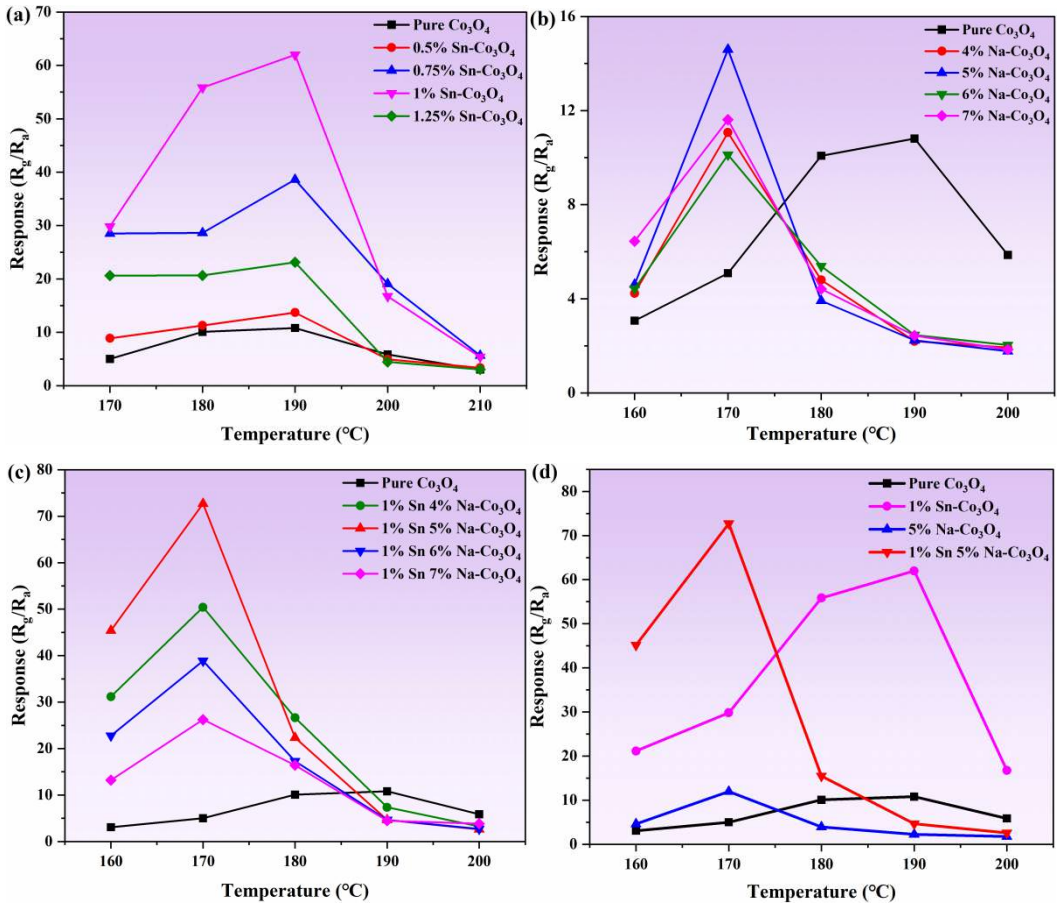


Fig. 8. Responses of (a) Sn-Co_3O_4 sensors with different Sn contents to 100 ppm TEA at 170-210 °C; (b,c) Na-Co_3O_4 and Sn/Na-Co_3O_4 sensors with different doping contents to 100 ppm TEA at 160-200 °C; and (d) pure Co_3O_4, 1%Sn-Co_3O_4, 5%Na-Co_3O_4, and 1%Sn5%Na-Co_3O_4 sensors to 100 ppm TEA at 160-200 °C.

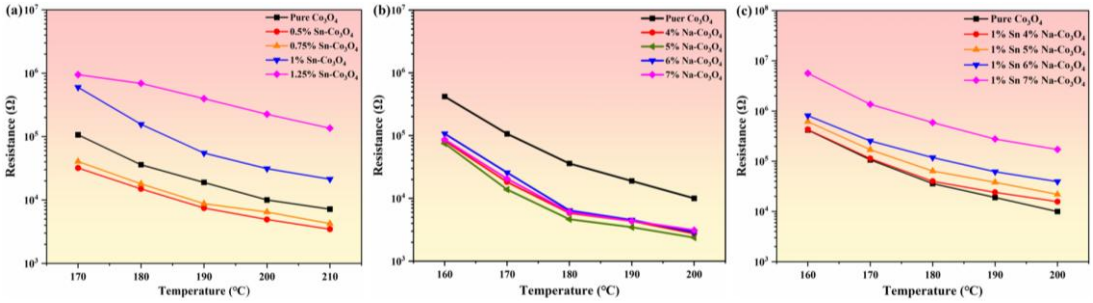


Fig. 9. (a-c) Resistance of all sensors at different operating temperatures to 100 ppm TEA.

The repeatability tests of pure Co_3O_4, 1%Sn-Co_3O_4, 5%Na-Co_3O_4 and 1%Sn5%Na-Co_3O_4 sensors at their optimal operating temperatures are measured in Fig. 10(a). All sensors undergo continuous cyclic response/recovery testing and achieve their respective maximum response values in five consecutive "air–TEA" cycle tests. Furthermore, during the continuous cycling tests, the variation in response values for each sample does not exceed 5%, indicating that the sensors exhibit good repeatability. Fig. 10(b) shows the response and recovery curves of the four samples for TEA concentrations ranging from 5 to 150 ppm at their optimal operating temperatures. Based on the changes in TEA concentration, the linear fitting curves for the response values are obtained

in Fig. 10(c). The determination coefficients R^2 of the pure Co_3O_4, 1%Sn-Co_3O_4, 5%Na-Co_3O_4 and 1%Sn5%Na-Co_3O_4 sensors are 0.975, 0.988, 0.970 and 0.986, respectively. The linear equation for the 1%Sn5%Na-Co_3O_4 sensor is y=0.61x+3.02. The theoretical detection limit is calculated using the following equation[29].

$$LOD(ppm)=\frac{3\sigma}{S} \quad (1)$$

σ is the root-mean-square error of the sensor, which indicates the variability in the sensor's baseline response; S is the slope of the linear fit equation, with a value of 0.61.

$$\sigma=\sqrt{\frac{1}{N}\sum_{i=1}^{N}(X_i-\overline{X})^2} \quad (2)$$

X_i, $\overline{X}$, and N represent the reference value, the average value, and the number of data points, respectively. According to the formula, the *LOD* for the 1%Sn5%Na-Co_3O_4 sample for TEA gas is 1.48 ppm.

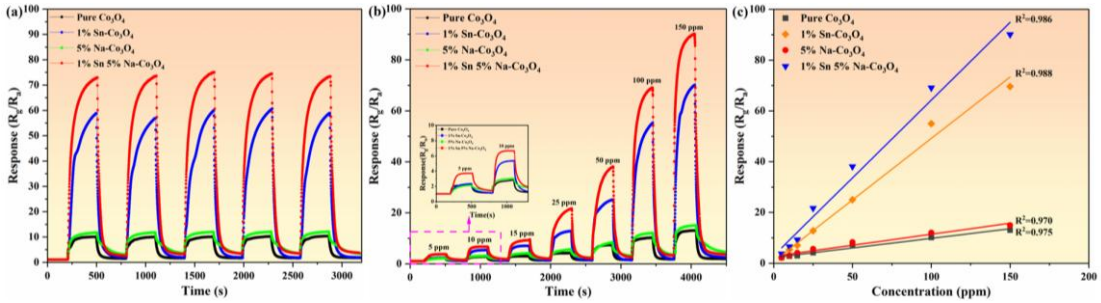


Fig. 10. (a) Repeatability of pure Co_3O_4, 1%Sn-Co_3O_4, 5%Na-Co_3O_4, and 1%Sn5%Na-Co_3O_4 sensors during five continuous exposure cycles to 100 ppm TEA gas at their optimum operating temperatures; (b) responses of these four sensors to 5-150 ppm TEA gas at their optimum operating temperatures; (c) linear fitting of these four sensors toward different concentrations of TEA gas.

The response/recovery times are important parameters for evaluating the dynamic sensing characteristics of gas sensors. The response time is defined as the required time for the response signal to reach 90% of steady-state change after exposure to TEA, whereas the recovery time is the required time for the signal to return 10% of its total change after TEA is removed[30]. As shown in Fig. 11(a-d), the response/recovery times of pure Co_3O_4, 1%Sn-Co_3O_4, 5%Na-Co_3O_4 and 1%Sn5%Na-Co_3O_4 sensors toward 100 ppm TEA are 73/70, 173/64, 100/374 and 130/63 s, respectively. Compared with pure Co_3O_4, the 1%Sn-Co_3O_4 sensor exhibits a longer response time but a slightly shorter recovery time. The prolonged response process may be associated with the increased number of adsorption and reaction sites induced by Sn doping, which allows more TEA molecules to participate in the surface reaction. Meanwhile, the regulation of surface defects and oxygen adsorption by Sn doping may facilitate the desorption of reaction products and the restoration of surface-adsorbed oxygen, thereby shortening the recovery time[31]. The 5%Na-Co_3O_4 sensor shows a markedly prolonged recovery time of 374 s, which may mainly result from its relatively low operating temperature of 170 °C. At this temperature, the desorption of TEA molecules and reaction products is kinetically limited, leading to slow recovery. Although the 1%Sn5%Na-Co_3O_4 sensor also operates at 170 °C, it exhibits a recovery time of only 63 s. This result indicates that Sn/Na co-doping effectively alleviates the slow recovery caused by Na

doping alone, enabling the sensor to maintain a relatively balanced response and recovery behavior at a lower operating temperature.

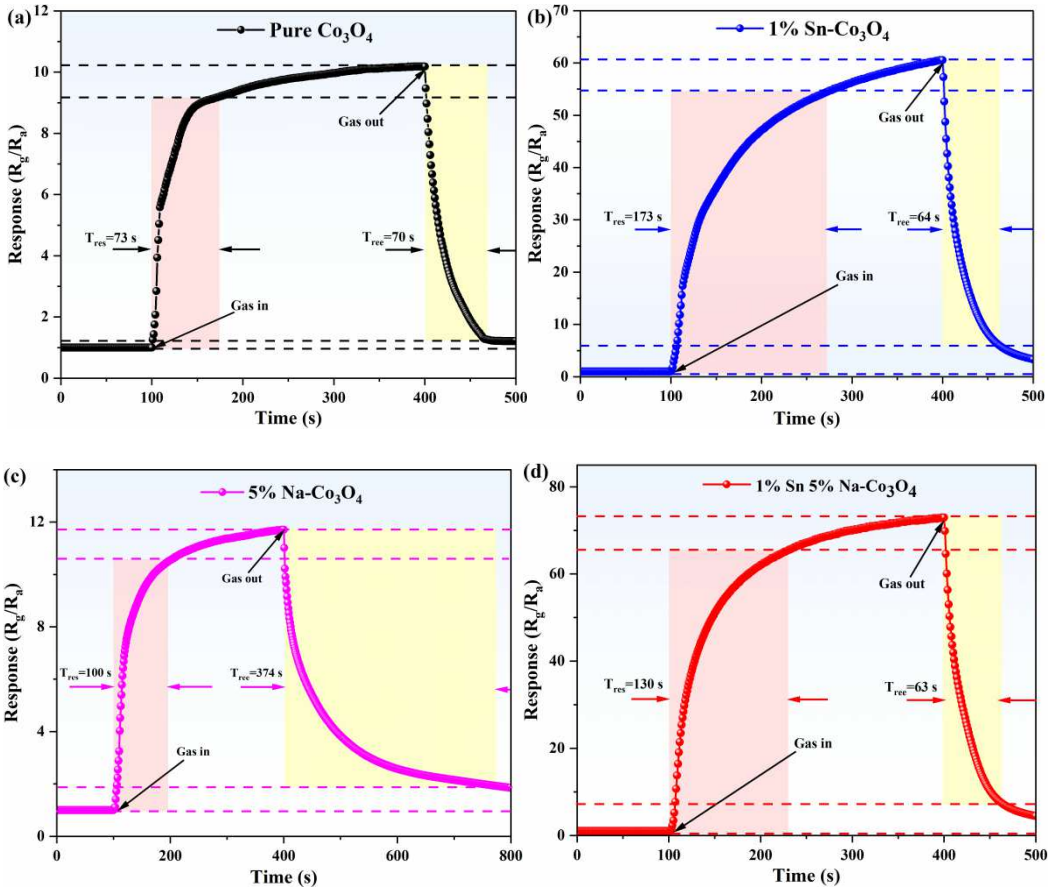


Fig. 11. Response/recovery curves of (a) pure Co_3O_4; (b) 1%Sn-Co_3O_4; (c) 5%Na-Co_3O_4; (d) 1%Sn5%Na-Co_3O_4.

Selectivity is a key performance parameter for gas sensors, which is used to measure a sensor's ability to identify a target gas in the presence of various interfering gases[32]. As shown in Fig. 12(a), at the optimal operating temperature, the 1%Sn5%Na-Co_3O_4 sensor was tested against six common VOCs: ethylene glycol, trimethylamine, ethanol, methanol, acetone and TEA. The response of the 1%Sn5%Na-Co_3O_4 sensor to TEA was significantly higher than that to other interfering gases, indicating good selectivity and resistance to interference for TEA. Fig. 12(b) shows the results of a 30-day stability test conducted on the 1%Sn5%Na-Co_3O_4 sensor toward TEA gas at 170 ℃. The response values of 1%Sn5%Na-Co_3O_4 sensor to TEA gas show almost no significant decay with the overall response remaining stable. It indicates that the sensor possesses good long-term stability.

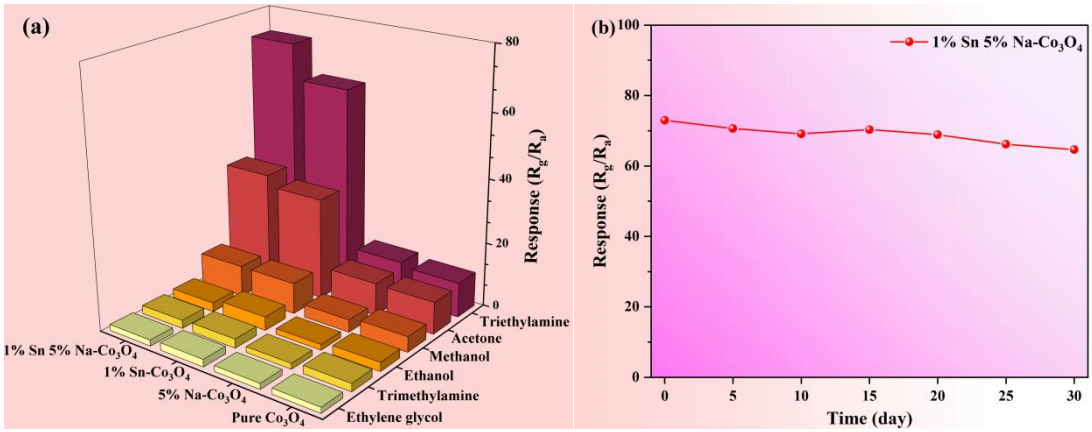


Fig. 12. (a) Response of pure Co_3O_4, 1%Sn-Co_3O_4, 5%Na-Co_3O_4, and 1%Sn5%Na-Co_3O_4 sensors to different VOCs; (b) Long-term stability of the 1%Sn5%Na-Co_3O_4 sensor toward 100 ppm TEA gas at 170 ℃.

In humid environments, H_2O molecules will compete with the target gas for surface adsorption sites and react with chemisorbed oxygen to form hydroxyl groups, thereby hindering charge transport and gas diffusion[33]. It will lead to a decline in sensor response. Therefore, humidity variation tests are conducted on pure Co_3O_4 and 1%Sn5%Na-Co_3O_4 sensor. The response of both sensors decreases as humidity increasing in Fig. 13(a). The decrease percentage of response is illustrated at different relative humidities in Fig. 13(b). Under 80% relative humidity conditions, the response values of the pure Co_3O_4 and 1%Sn5%Na-Co_3O_4 sensors decrease to 44.79% and 72.44%, respectively. The 1%Sn5%Na-Co_3O_4 sensor exhibits better gas-sensing performance under high-humidity conditions. The possible reason attributes to the multivalent nature of Co^{2+} and Co^{3+} in Co_3O_4[34]. As an important surface active site, Co^{2+} ion can promote the adsorption and activation of oxygen molecules and facilitate the formation of oxygen vacancies. On the other hand, the Co^{3+} ion primarily participates the Co^{2+}/Co^{3+} valence state cycle. The Co^{2+}-O-Co^{3+} active structure helps to maintain surface charge balance[35,36]. The introduction of Sn^{4+} modulates the electron density around Co ions, which influence the electron transfer process between Co^{2+} and Co^{3+}. The process can retain strong oxygen adsorption and activation capabilities of the surface. Consequently, the 1%Sn5%Na-Co_3O_4 sensor maintains a high and stable response even under high-humidity conditions.

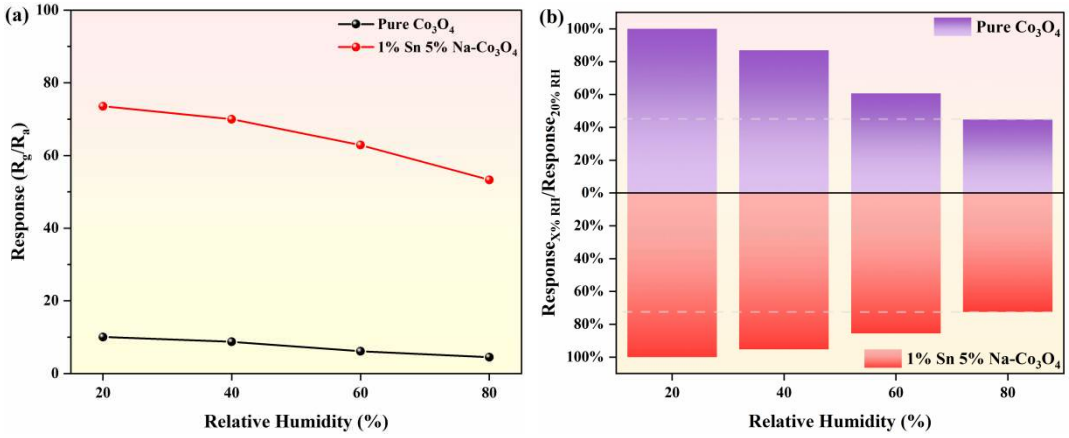


Fig. 13. (a) Responses of pure Co_3O_4 and 1%Sn5%Na-Co_3O_4 sensors to TEA gas under different relative humidity

conditions; (b) percentage decrease in the response of the two samples to TEA gas under different relative humidity conditions.

3.3 Gas sensing mechanism

The Co_3O_4 belongs to p-type semiconductor. Its gas-sensing response primarily stems from redox reactions between target gas molecules and adsorbed oxygen species on the material's surface, as well as the resulting changes in surface carrier concentration[37,38]. The mechanism diagrams for 1%Sn5%Na-Co_3O_4 in air and in TEA are shown in Fig. 14(a-b). When the 1%Sn5%Na-Co_3O_4 sensor is exposed to air, oxygen molecules first adsorb onto the material surface and capture electrons from it. Then it induces to form chemisorbed oxygen species such as O_2^- or O^-. The primary charge carriers in Co_3O_4 are holes. The chemisorbed oxygen will increase the hole concentration on the material. At last the hole accumulation layer is formed. The process can be represented as[39]:

$$O_2(gas) \rightarrow O_2(ads) \quad (3)$$

$$O_2(ads)+e^- \rightarrow O_2^-(ads)\ (T < 100\ ℃) \quad (4)$$

$$O_2^-(ads)+e^- \rightarrow 2O^-(ads)\ (100\ ℃ < T < 300\ ℃) \quad (5)$$

When the sensor is exposed to TEA gas, TEA belongs to a reducing gas. It reacts with adsorbed oxygen species on the surface of the 1%Sn5%Na-Co_3O_4. The production includes CO_2, H_2O and N_2. As same time, the electrons are simultaneously released to the surface of the 1%Sn5%Na-Co_3O_4 and recombined with holes. The result induces the decrease of hole concentration and a thinner hole accumulation layer, which in turn increases the material's resistance. The reaction process can be approximated as follows[40]:

$$2C_6H_{15}N\ (ads)+39O^-\ (ads) \rightarrow 12CO_2+15H_2O+N_2+39e^- \quad (6)$$

$$4C_6H_{15}N\ (ads)+39O_2^-\ (ads) \rightarrow 24CO_2+30H_2O+2N_2+39e^- \quad (7)$$

Fig. 14(c-d) shows the changes in the energy bands and the hole accumulation layer of the 1%Sn5%Na-Co_3O_4 sample in air and in TEA gas, respectively.

In addition, the 1%Sn5%Na-Co_3O_4 sensor exhibits a higher response to TEA gas. The BET test results indicate that the co-doping of Sn and Na increases the specific surface area of the Co_3O_4 material and the number of active sites on its surface. The larger specific surface area provides more adsorption and reaction sites for oxygen and TEA molecules. At the same time, the introduction of Sn and Na also can induce the lattice distortion and charge imbalance, which promote the formation of surface defects such as oxygen vacancies. According to XPS analysis results, the content of oxygen vacancies and adsorbed oxygen of 1%Sn5%Na-Co_3O_4 is higher than that of pure Co_3O_4. The dopant of Sn and Na can enhance the surface oxygen adsorption and activation capabilities. So, the enhancement of gas-sensing performance for 1%Sn5%Na-Co_3O_4 attributes to an increase in specific surface area, a higher concentration of oxygen vacancies, an increase in active sites and enhanced surface redox reactivity.

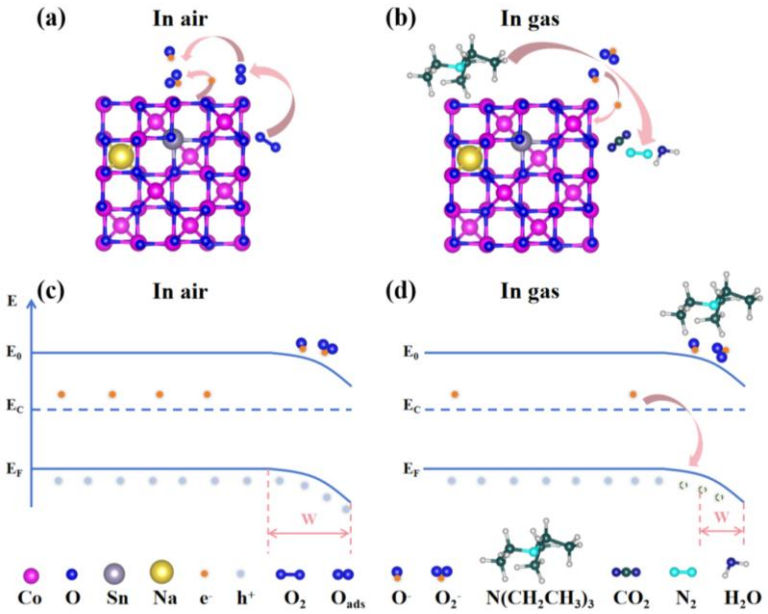


Fig. 14. Schematic diagram of the gas-sensing mechanism of the 1%Sn5%Na-Co_3O_4 sensor toward TEA gas.

4. Conclusions

In this study, the pure Co_3O_4, Sn-Co_3O_4, Na-Co_3O_4 and Sn/Na-Co_3O_4 nanospheres are successfully synthesized through one-step solvothermal method. The crystal structure, morphology, elemental distribution, surface chemical composition and specific surface area of the samples are systematically characterized by XRD, SEM, TEM, XPS and BET. The sensing performance toward TEA is systematically investigated. The test results show that the optimal operating temperature of the 1%Sn5%Na-Co_3O_4 sensor for 100 ppm TEA is 20 ℃ lower than that of pure Co_3O_4, while its response value is approximately 7.2 times higher. The theoretical detection limit of the 1%Sn5%Na-Co_3O_4 sensor is calculated to be approximately 1.48 ppm. The sensor also exhibits good anti-humidity and long-term stability. This study provides an effective strategy for developing highly sensitive, relatively low-operating-temperature, low-detection-limit, stable and reliable Co_3O_4-based TEA gas sensors and demonstrates potential application value in food safety for the early identification of fish spoilage and rapid freshness assessment.

CRediT authorship contribution statement

Yuhong Zhang: Writing – review & editing. **Junnan Liu:** Writing – original draft, Investigation. **Haoran Niu:** Methodology, Investigation. **Juncheng Li:** Formal analysis, Data curation. **Mingzhe Cui:** Investigation. **Hang Liu**: Data curation, Conceptualization.

Declaration of competing interest

We declare that we do not have any commercial or associative interest that represents a conflict of interest in connection with the work submitted.

Acknowledgments

This work was supported by Project of Jilin Provincial Science and Technology Department (No:20250203093SF).

References

[1] K.A. Byrd, S.H. Thilsted, K.J. Fiorella, Fish nutrient composition: a review of global data from poorly assessed inland and marine species, Public Health Nutr. 24 (2021) 476–486, https://doi.org/10.1017/S1368980020003857.

[2] X.B. Nie, R.C. Zhang, L.L. Cheng, W.B. Zhu, S.L. Li, X.M. Chen, Mechanisms underlying the deterioration of fish quality after harvest and methods of preservation, Food Control 135 (2022) 108805, https://doi.org/10.1016/j.foodcont.2021.108805.

[3] T. Ding, Y.L. Li, Biogenic amines are important indices for characterizing the freshness and hygienic quality of aquatic products: A review, LWT 194 (2024) 115793, https://doi.org/10.1016/j.lwt.2024.115793.

[4] W. Wang, J. Fang, Y.Z. Fan, Q.L. Wang, Y. Chen, S.P. Ruan, The regulation of ZIF-derived ZnO nanocages by Yb_2O_3 for high-performance triethylamine sensing and fish freshness assessment, Talanta 288 (2025) 127757, https://doi.org/10.1016/j.talanta.2025.127757.

[5] Z.H. Zhao, S.H. Chen, H.Q. Li, L. Wu, Z.G. Shao, Q.L. Zou, Z.K. Wang, Flower-like $FeWO_4$/f-MWCNTs Sphere for Triethylamine Gas Sensors Operating at Room Temperature: Sensing Performance, Mechanism Study, and Application to Detection of Fish Freshness, ACS Sens. 10 (2025) 7456–7474, https://doi.org/10.1021/acssensors.5c01416.

[6] Y.T. Huang, L.Y. Fan, Y.F. Liu, X.H. Zheng, High-performance MoO_3 nanosheets gas sensors for triethylamine detection: A rapid approach for assessing fish freshness, Ceramics International 51 (2025) 9912–9922, https://doi.org/10.1016/j.ceramint.2024.12.423.

[7] M.N. Madhubhashini, C.P. Liyanage, A.U. Alahakoon, R.P. Liyanage, Current applications and future trends of artificial senses in fish freshness determination: A review, J. Food Sci. 89 (2024) 33–50, https://doi.org/10.1111/1750-3841.16865.

[8] L. Liu, Y.Y. Wang, Y.H. Liu, S.Q. Wang, T. Li, S.M. Feng, S.J. Qin, T. Zhang, Heteronanostructural metal oxide-based gas microsensors, Microsyst. Nanoeng. 8 (2022) 85, https://doi.org/10.1038/s41378-022-00410-1.

[9] L.Y. Liu, C.L. Mao, H.Y. Fu, X.L. Qu, S.R. Zheng, ZnO nanorod-immobilized Pt single-atoms as an ultrasensitive sensor for triethylamine detection, ACS Appl. Mater. Interfaces 15 (2023) 16654–16663, https://doi.org/10.1021/acsami.2c21410.

[10] Y.H. Gui, K. Tian, J.X. Liu, L.L. Yang, H.Z. Zhang, Y. Wang, Superior triethylamine detection at room temperature by {−112} faceted WO_3 gas sensor, J. Hazard. Mater. 380 (2019) 120876, https://doi.org/10.1016/j.jhazmat.2019.120876.

[11] X.Y. Liu, D.Z. Yang, Y.L. Guo, F. Wang, D.Q. Han, Z.G. Kan, C.L. Li, Room temperature triethylamine gas sensor with excellent performances based on novel porous CuO foam via a simple and facile route, Sens. Actuators B: Chem. 390 (2023) 133934, https://doi.org/10.1016/j.snb.2023.133934.

[12] G.W.C. Kumarage, E. Comini, Low-Dimensional Nanostructures Based on Cobalt Oxide (Co_3O_4) in Chemical-Gas Sensing, Chemosensors 9 (2021) 197, https://doi.org/10.3390/chemosensors9080197.

[13] D.H. Kong, J.Y. Han, Y.B. Gao, Y. Gao, W.R. Zhou, G.N. Liu, G.Y. Lu, Lower coordination Co_3O_4 mesoporous hierarchical microspheres for comprehensive sensitization of triethylamine vapor sensor, J. Hazard. Mater. 430 (2022) 128469, https://doi.org/10.1016/j.jhazmat.2022.128469.

[14] Q. Ding, H.R. Li, W.N. Liu, D.D. Huang, X. Tan, M.Y. Zhao, Q.L. Cheng, M. Yi, Y.Q. Ren,

Fast response triethylamine sensor based on MOF-derived coral flower-like Fe-doped Co_3O_4, Mater. Sci. Semicond. Process. 180 (2024) 108557, https://doi.org/10.1016/j.mssp.2024.108557.

[15] D.T.T. Le, V.A. Tuan, M. Tonezzer, C.M. Hung, N.D. Hoa, An electrospinning deposited cobalt oxide nanofiber gas sensing device: selective enhancement as a thermal electronic nose, RSC Adv. 15 (2025) 15293–15301, https://doi.org/10.1039/D5RA00873E.

[16] Z.L. Zhang, P.P. Qiu, Y.H. Deng, W. Luo, Recent Advances in Functionalizing Metal Oxide Semiconductors for Highly Sensitive Gas Sensors, Small Methods 9 (2025) 2500228, https://doi.org/10.1002/smtd.202500228.

[17] K. Zhang, P.G. Tang, Y.J. Feng, D.Q. Li, Novel strategy to prepare mesoporous Sn-doped Co_3O_4 whiskers with high sensitivity to toluene, Ind. Eng. Chem. Res. 59 (2020) 4472–4482, https://doi.org/10.1021/acs.iecr.9b06001.

[18] R. Saad, K. Abdelkarem, A.M. El Sayed, M. Shaban, I.A. Ahmed, M.T. Tammam, H. Hamdy, Characterization and enhanced carbon dioxide sensing performance of spin-coated Na- and Li-doped and Co-doped cobalt oxide thin films, RSC Adv. 14 (2024) 36852–36867, https://doi.org/10.1039/D4RA06847E.

[19] G.A. Begaw, A.K. Worku, D.W. Ayele, T.A. Yemata, T.A. Wubieneh, M.A. Teshager, F.A. Yihun, Enhancing Thermal Properties of Co_3O_4 Nanoparticles Through Optimized Mn-Doping Concentrations, Int. J. Electrochem. (2024) 7343751, https://doi.org/10.1155/ijel/7343751.

[20] R.R. Jin, Y.R. Jiang, L.P. Zhao, T.S. Wang, X.M. Liu, F.M. Liu, X. Yan, P. Sun, G.Y. Lu, High sensitivity and low detection limit of acetone sensor based on Ru-doped Co_3O_4 flower-like hollow microspheres, Sens. Actuators B Chem. 363 (2022) 131839, https://doi.org/10.1016/j.snb.2022.131839.

[21] X.H. Ji, X. Wang, Q. Zhang, S.Y. Liu, Y.Y. Lin, Z.H. Deng, K. Nagashima, Y. He, C.Y. Shen, G. Meng, Sn-doped Co_3O_4 nanosheet based isoprene sensor for dynamic metabolic monitoring, ACS Sensors 11 (2026) 7404–7413, https://doi.org/10.1021/acssensors.6c01772.

[22] A. Rossi, B. Fabbri, E. Spagnoli, A. Gaiardo, M. Valt, M. Ferroni, M. Ardit, S. Krik, A. Pedrielli, L. Vanzetti, V. Guidi, Functionalization of Indium Oxide for Empowered Detection of CO_2 over an Extra-Wide Range of Concentrations, ACS Appl. Mater. Interfaces 15 (2023) 33732–33743, https://doi.org/10.1021/acsami.3c04789.

[23] R.D. Su, Y.X. Gao, L. Chen, Y. Chen, N. Li, W. Liu, B.Y. Gao, Q. Li, Utilizing the oxygen-atom trapping effect of Co_3O_4 with oxygen vacancies to promote chlorite activation for water decontamination, Proceedings of the National Academy of Sciences 121 (2024) e2319427121, https://doi.org/10.1073/pnas.2319427121.

[24] C. Zhang, G.F. Liu, X. Geng, K.D. Wu, M. Debliquy, Metal oxide semiconductors with highly concentrated oxygen vacancies for gas sensing materials: A review, Sens. Actuators A Phys. 309 (2020) 112026, https://doi.org/10.1016/j.sna.2020.112026.

[25] J.Y. Li, E.T. Na, X.D. Liang, Q.H. Liang, M.H. Fan, H. Chen, G.D. Li, X.X. Zou, Surface oxygen chemistry of metal oxide semiconductors for gas-sensing applications, Inorg. Chem. Front. 11 (2024) 8602–8626, https://doi.org/10.1039/D4QI02385D.

[26] Q.J. Fu, M.M. Ai, Y. Duan, L.M. Lu, X. Tian, D.D. Sun, Y.Y. Xu, Y.Q. Sun, Synthesis of uniform porous NiO nanotetrahedra and their excellent gas-sensing performance toward formaldehyde, RSC Adv. 7 (2017) 52312–52320, https://doi.org/10.1039/C7RA10730G.

[27] H.M. Sun, L. Liu, Metal-Organic frameworks-derived 2D spindle-like Sn-doped Co_3O_4 porous nanosheets as efficient materials for TEA detection, Sens. Actuators B: Chem. 338 (2021) 129825, https://doi.org/10.1016/j.snb.2021.129825.

[28] C. Qin, Z.X. Wei, B. Wang, Y. Wang, Sn and Mn co-doping synergistically promotes the sensing properties of Co_3O_4 sensor for high-sensitive CO detection, Sensors and Actuators B: Chemical 390 (2023) 133930, https://doi.org/10.1016/j.snb.2023.133930.

[29] F.D. Qu, Y. Yuan, R. Guarecuco, M.H. Yang, Low working-temperature acetone vapor sensor based on zinc nitride and oxide hybrid composites, Small 12 (2016) 3128–3133, https://doi.org/10.1002/smll.201600422.

[30] N.A. Isaac, I. Pikaar, G. Biskos, Metal oxide semiconducting nanomaterials for air quality gas sensors: operating principles, performance, and synthesis techniques, Microchim. Acta 189 (2022) 196, https://doi.org/10.1007/s00604-022-05254-0.

[31] R. Saad, K. Abdelkarem, M. Shaban, A.M. El Sayed, I.A. Ahmed, M.T. Tammam, H. Hamdy, Highly sensitive and room-temperature operable carbon dioxide gas sensor based on spin-coated Sn-doped Co_3O_4 thin films with advanced recovery properties, Surf. Interfaces 55 (2024) 105309, https://doi.org/10.1016/j.surfin.2024.105309.

[32] M. Wusiman, F. Taghipour, Methods and mechanisms of gas sensor selectivity, Critical Reviews in Solid State and Materials Sciences 47 (2022) 416–435, https://doi.org/10.1080/10408436.2021.1941752.

[33] Y.J. Wang, Y. Zhou, Recent Progress on Anti-Humidity Strategies of Chemiresistive Gas Sensors, Materials 15 (2022) 8728, https://doi.org/10.3390/ma15248728.

[34] O. Yurchenko, P. Diehle, F. Altmann, K. Schmitt, J. Wöllenstein, Co_3O_4-Based Materials as Potential Catalysts for Methane Detection in Catalytic Gas Sensors, Sensors 24 (2024) 2599, https://doi.org/10.3390/s24082599.

[35] S. Vladimirova, V. Krivetskiy, M. Rumyantseva, A. Gaskov, N. Mordvinova, O. Lebedev, M. Martyshov, P. Forsh, Co_3O_4 as p-Type Material for CO Sensing in Humid Air, Sensors 17 (2017) 2216, https://doi.org/10.3390/s17102216.

[36] D.H. Kong, W.R. Zhou, J.Y. Han, Y.B. Gao, Y. Gao, L.P. Zhao, P. Sun, G.Y. Lu, Mesoporous Co_3O_4 nanosheets with exposed Co^{2+}-rich crystal facets for improved toluene detection, Applied Surface Science 619 (2023) 156714, https://doi.org/10.1016/j.apsusc.2023.156714.

[37] J.M. Xu, J.P. Cheng, The advances of Co_3O_4 as gas sensing materials: A review, Journal of Alloys and Compounds 686 (2016) 753–768, https://doi.org/10.1016/j.jallcom.2016.06.086.

[38] X.X. He, H.F. Chai, Y.W. Zhou, K.W. Liu, Z.X. Yu, C. Zhang, Sensing properties and mechanisms of LaF_3–Co_3O_4 nanorods for low-concentration methanol detection, Rare Metals 43 (2024) 2193–2204, https://doi.org/10.1007/s12598-023-02593-6.

[39] H. Liu, Z.H. Qu, Y.C. Liu, J.L. Liu, S.Y. Tian, Y.H. Zhang, High performance and low detection limit isopropanol gas sensor based on 3D $ZnSnO_3$ nanocubes co-catalyzed by Au nanoparticles and ZrO_2, J. Alloys Compd. 1006 (2024) 176276, https://doi.org/10.1016/j.jallcom.2024.176276.

[40] T.T. Xu, H.R. Wang, J. Zhao, F.B. Zhao, W.B. Cong, G.L. Wang, J.Q. Li, Biotemplate synthesis of a Co_3O_4 microtube sensor for fast triethylamine detection, Dalton Transactions 52 (2023) 10835–10843, https://doi.org/10.1039/D3DT01450A.

Supplementary Files

This is a list of supplementary files associated with this preprint. Click to download.

- Appendix.docx